CHAPTER 3

Results and Discussion

The content in this chapter is divided into 3 major parts. The aim of each experimental part is as follows**.**

3.1 To investigate the photocatalytic MB degradation activities and the characteristic properties of pure Ag_3VO_4, pure $CoTiO_3$ and $Ag_3VO_4/CoTiO_3$ composites by XRD, SEM, UV-vis DRS, XPS, FTIR, TEM, XRF and PL studies.

3.2 To understand the enhanced photocatalytic properties of the coupling system in term of the energy band alignment between the two semiconductors in $Ag_3VO_4/CoTiO_3$ composite by XPS technique. Therefore, the band energy diagram is proposed to explain the photocatalytic improvement of the heterostructured system.

3.3 To investigate the functions of Ag_3VO_4 and $CoTiO_3$ in the composite catalyst and to identify the main active species in the photocatalytic degradation of MB over the catalysts being studied.

It is expected that details on characteristic properties and energy band diagram of the photocatalyst as well as the possible main active species obtained in this studied would help explain the enhanced photocatalytic activity as observed and might lead to the design of novel catalyst for complex organic pollutant degradation.

3.1 Characteristic properties of photocatalysts

3.1.1 X-ray diffraction (XRD) characterization

The phase purity was identified by XRD characterization. The XRD pattern of pure Ag_3VO_4, $CoTiO_3$ and composites are compared with JCPDS file (Joint Committee for Powder Diffraction Standards) to find the correlated peak pattern. $CoTiO_3$ corresponds with JCPDS no. 15-0866 [1-5], while Ag_3VO_4 accords with JCPDS no. 43-0542 [6-7]. The results of various $Ag_3VO_4/CoTiO_3$ ratios are shown in Fig. 3.1.

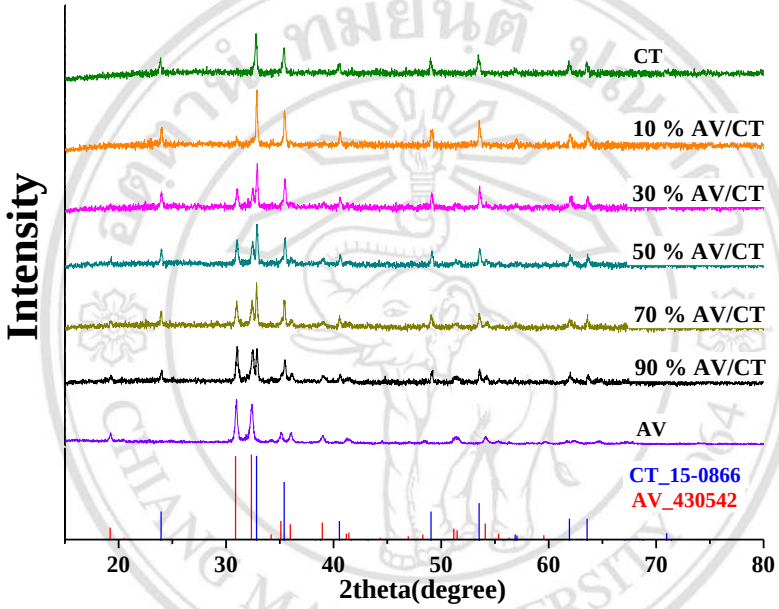

Fig. 3.1 X-ray diffraction patterns of obtained materials and their corresponding JCPDS files.

In Fig. 3.1, CT is referred to $CoTiO_3$ whereas AV is referred to Ag_3VO_4. As seen from the figure, all peaks from $CoTiO_3$ and Ag_3VO_4 correspond to JCPDS file no. 15-0866 and 43-0542, respectively. For $CoTiO_3$ the XRD peaks at 23.9°, 32.8°, 35.3°, 40.4°, 49.0°, 53.5°, 61.9° and 63.5° relate to the (012), (104), (110), (113), (024), (116), (214) and (300) planes of ilmenite $CoTiO_3$. The peaks of Ag_3VO_4 at 19.2°, 30.9°, 32.4°, 35.1°, 36.0°, 39.0°, 41.4°, 48.3°, 51.2°, 51.3° and 54.2° are ascribed to the (011), (-121), (121), (301), (202), (022), (400), (-322), (132), (-330) and (331) planes of monoclinic Ag_3VO_4. No impurity phase is found from both materials, indicating that the synthesis conditions used in this study can provide $CoTiO_3$ and Ag_3VO_4 with high purity.

For the composite materials, various weight ratios between Ag_3VO_4 and $CoTiO_3$ are synthesized e.g. 10% w/w, 30% w/w, 50% w/w, 70% w/w and 90% w/w of $Ag_3VO_4/CoTiO_3$. It was found that both phases are apparent in composite materials. Moreover, there is a significant rise of peak intensity of Ag_3VO_4 component, while the intensity of $CoTiO_3$ peaks are reduced when increasing amount of Ag_3VO_4 in the composite. This is become the intensity of XRD patterns is related to mass fraction of constituent compound in composite materials. Therefore, increasing amount of one phase in composite leads to a decrease in peak intensity of another phase [8-9]. Since no impurity phase is observed from composites in all compositions, the method used for composite formation in this study is therefore considered as an appropriate method.

In addition, XRD results can be used to estimate the crystallite size of the particle according to the Scherrer's equation in Eq. 3.1.

$$L = \frac{K\lambda}{\beta \cos\theta} \tag{3.1}$$

where L = Crystallite size (nm)

λ = Wavelength of X-ray radiation (Cu Kα = 0.1541 nm)

K = Scherrer shape factor (as 0.90 for $CoTiO_3$ [1,3], as 0.94 for Ag_3VO_4 [7])

β = Line width at half maximum height (FWHM) (radians)

θ = Diffraction angle at maximum intensity

For evaluation of crystallite size, the highest intensity usually found in low angle of diffraction is an appropriated peak for measuring the full width at half maximum (FWHM), since it exemplifies the whole crystalline powders [10].

In Fig. 3.2, FWHM of about 0.19 degrees at 32.78 degrees of 2theta of $CoTiO_3$ is found. The corresponding crystallite size is calculated as shown below.

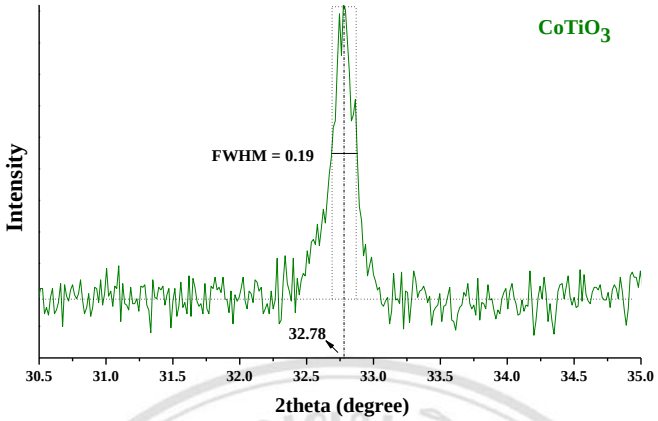

Fig. 3.2 FWHM estimation from XRD pattern to calculate crystallite size of $CoTiO_3$.

$$L = \frac{0.90 \times 0.1541(nm)}{\left[\left(0.19 \times \frac{\pi}{180}\right)(rads)\right]\left[\cos\left(\frac{32.78}{2}\right)\right]}$$

$$L = 44 \text{ nm}$$

Similarly, the FWHM estimation in the case of Ag_3VO_4 is shown in Fig. 3.3 and the crystallite size calculation is presented below.

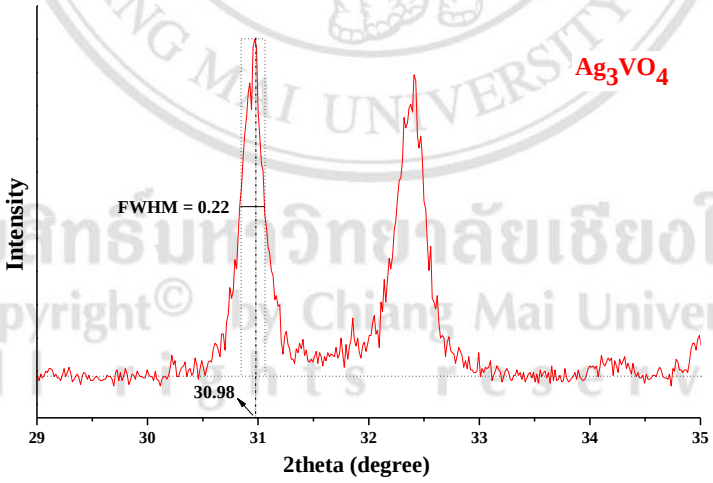

Fig. 3.3 FWHM estimation from XRD pattern to calculate crystallite size of Ag_3VO_4.

$$L = \frac{0.94 \times 0.1541(nm)}{\left[\left(0.22 \times \frac{\pi}{180}\right)(rads)\right]\left[\cos\frac{30.98}{2}\right]}$$

$$L = 39 \text{ nm}$$

The lattice parameter and the volume of unit cell of $CoTiO_3$ component can be calculated by using the planes of high intense peak with narrow FWHM for accurate calculation as shown in Table 3.1.

Table 3.1 Details on XRD patterns of $CoTiO_3$ and Ag_3VO_4 for calculation of cell parameters and unit cell volume of each constituent materials.

$CoTiO_3$			**Ag_3VO_4**		
hkl	2theta (*2θ*)	*d(Å)*	*hkl*	2theta (*2θ*)	*d(Å)*
104	32.8	2.7304	011	19.2	4.6225
110	35.3	2.5426	301	35.1	2.5566
			$\bar{3}30$	51.3	1.7809

The planes of (104) and (110) are used in the following eqation (Eq. 3.2).

Hexagonal crystal system of $CoTiO_3$;

$$\frac{1}{d^2} = \frac{4}{3}\left[\frac{h^2 + hk + k^2}{a^2}\right] + \frac{l^2}{c^2} \tag{3.2}$$

(104) plane

$$\frac{1}{(2.7304)^2} = \frac{4}{3}\left[\frac{1^2 + (1)0 + 0^2}{a^2}\right] + \frac{4^2}{c^2}$$

$$0.1341 = \frac{4}{3a^2} + \frac{16}{c^2} \tag{3.2.1}$$

(110) plane

$$\frac{1}{(2.5426)^2} = \frac{4}{3}\left[\frac{1^2 + (1)(1) + 1^2}{a^2}\right] + \frac{0^2}{c}$$

$$a^2 = 25.8593$$

$$a = 5.0852$$

Substituted lattice parameter (a) in Eq. 3.2.1 to obtain;

$$0.1344 = \frac{4}{3(5.0852)^2} + \frac{16}{c^2}$$

$$c = 13.8977 \text{ Å}$$

Therefore, the volume of unit cell equals to $\frac{\sqrt{3}a^2c}{2} = \frac{\sqrt{3}(5.0852)^2(13.8977)}{2} = 311.24$ Å^3

The lattice parameters and volume of unit cell of $CoTiO_3$ from the above calculation correspond well with the values provided in JCPDS no. 15-0866, so it can be concluded that the pure phase of $CoTiO_3$ is obtained.

Similarly, the lattice parameters and volume of unit cell of Ag_3VO_4 can also be calculated by using the equation of monoclinic system as in Eq. 3.3.

Monoclinic crystal system for Ag_3VO_4;

$$\frac{1}{d^2} = \frac{1}{\sin^2\beta}\left[\frac{h^2}{a^2} + \frac{k^2\sin^2\beta}{b^2} + \frac{l^2}{c^2} - \frac{2hl\cos\beta}{ac}\right] \tag{3.3}$$

(301) plane $$\frac{1}{(2.5566)^2} = \frac{1}{\sin^2(95.36)}\left[\frac{3^2}{a^2} + \frac{0^2\sin^2(95.36)}{b^2} + \frac{1^2}{c^2} - \frac{2(3)(1)\cos(95.36)}{ac}\right]$$

$$0.1353 = \frac{9}{a^2} + \frac{1}{c^2} \tag{3.3.1}$$

(011) plane $$\frac{1}{(4.6225)^2} = \frac{1}{\sin^2(95.36)}\left[\frac{0^2}{a^2} + \frac{1^2\sin^2(95.36)}{b^2} + \frac{1^2}{c^2} - \frac{2(0)(1)\cos(95.36)}{ac}\right]$$

$$c = \sqrt{\frac{1}{\left(0.0464 - \frac{0.9913}{b^2}\right)}} \tag{3.3.2}$$

Substitution of *c* value in Eq. 3.3.1 with that from Eq. 3.3.2 to obtain;

$$0.0888 = \left(\frac{9}{a^2} - \frac{0.9913}{b^2}\right) \tag{3.3.3}$$

(-330) plane

$$\frac{1}{(1.7809)^2} = \frac{1}{\sin^2(95.36)}\left[\frac{(-3)^2}{a^2} + \frac{3^2\sin^2(95.36)}{b^2} + \frac{0^2}{c^2} - \frac{2(-3)(0)\cos(95.36)}{ac}\right]$$

$$0.3125 = \left(\frac{9}{a^2} + \frac{8.9215}{b^2}\right) \tag{3.3.4}$$

Eq. 3.3.4-Eq. 3.3.3; $b = 6.6568$ Å

Substitution of *b* value in Eq. 3.3.3; $a = 8.9976$ Å

Substitution of *b* value in Eq. 3.3.2; $c = 6.4510$ Å

Thus, the volume of unit cell;

$$abc\sin\beta = (8.9976)(6.6568)(6.4510)\sin(95.36) = 384.69\ \text{Å}^3$$

The calculated value of lattice parameters and volume of unit cell of Ag_3VO_4 are similar to the values from JCPDS no. 43-0542, indicating that the pure phase of Ag_3VO_4 is presented.

3.1.2 Scanning electron microscope (SEM)

SEM is used to study surface morphology by detecting the secondary electron signal which can be detected within only a few micrometers from the surface. In Fig. 3.4, the morphologies of Ag_3VO_4, $CoTiO_3$ and composite are illustrated together with the energy dispersive X-ray spectrum (EDS) of the composite.

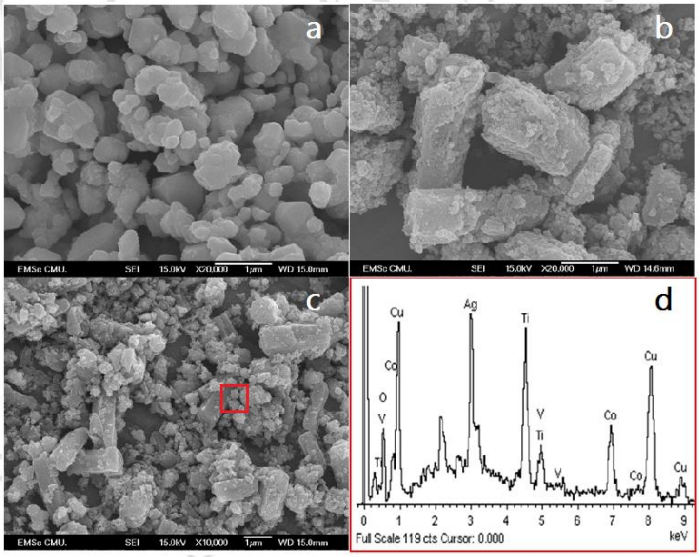

Fig. 3.4 Surface morphology of Ag_3VO_4 (a), $CoTiO_3$ (b), composite (c) and the EDS spectrum of composite (d).

Ag_3VO_4 is formed in an irregular shape by hydrothermal process with the size in the range of 0.3 to 1.2 μm. $CoTiO_3$ particle exhibits larger particle size which is between 2 to 4 μm in length and 0.5 to 1.2 μm in width. The $CoTiO_3$ shows the rod-like morphology with rough surface due to its high temperature calcination to form the pure

phase. The particle sizes from SEM characterization are compared with the crystallite sizes from XRD in Table 3.2. It can be seen from the table that the particle size from SEM technique is larger than the crystallite size obtained from XRD, possibly because the particle composes of an agglomerated amorphous phase at the outer but the crystal at the inside of the particle, so larger size is found from SEM analysis [11-12]. This can be verified from XRD pattern in Fig. 3.1. It can be clearly observed that there are many noise signals and low peak intensities apparent referred to amorphous phase formation in obtained materials.

The composite material in Fig. 3.4(c) shows both irregular shape of Ag_3VO_4 and rod-like shape of $CoTiO_3$ which are confirmed by EDS characterization in Fig. 3.4(d). The EDS result illustrates all of the elements that should be found in the composite material e.g. Ag, V, O, Co and Ti, indicating that both phases are presented in the composite. The existence of Cu element in EDS spectrum comes from the copper tape support.

Table 3.2 Size comparison between the calculated crystallite size form XRD and particle size from SEM measurement of each component.

Type	**Size of Ag_3VO_4 (nm)**	**Size of $CoTiO_3$ (nm)**
Crystallite size from calculation	44	39
Particle size from SEM Investigation	between 300 to 1200	between 500 to 1200

The rod-like shape of $CoTiO_3$ is produced via sol gel method by using ethylene glycol (EG) as a solvent. Since ethylene glycol is a bidentate ligand, it can react with metal ion to form metal-glycolate polymer chain-like structure which can coordinate with two transition metals. The chain-like structure of Co-Ti-EG bonds can further coagulate to form the rod-like shape by van der Waals interaction between each chain-like complex [5]. This rod-like formation process is related to our experimental procedures as follows.

It is found that, after adding TTIP in the mixed solution between cobalt acetate and ethylene glycol, cloudy pink suspension is formed within a few minutes. This cloudy pink suspension indicates the chain-like polymer formation as mentioned earlier. When ageing the suspension overnight, the gel-like pink suspension is produced. The

appearance of gel-like suspension is likely due to a high polymerization degree, resulting in the long length of polymer chain in the system. After that, the gel is calcined at 800 °C for 4 h under ambient air. During calcination process, the pyrolysis of the glycolate precursor is occurred and the surface morphology of $CoTiO_3$ is changed from smooth to rough. These steps of rod-like $CoTiO_3$ growth are exhibited in Fig. 3.5 [13-14].

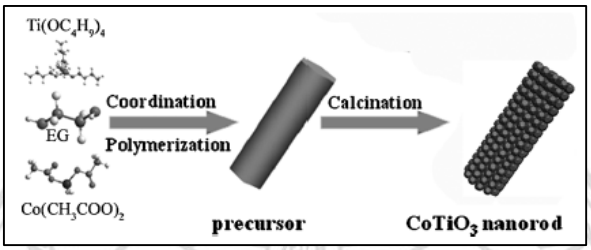

Fig. 3.5 The formation of rod-like $CoTiO_3$ via sol-gel method by using ethylene glycol as a solvent [5].

3.1.3 Photocatalytic testing

Photocatalytic activity was investigated in the black box for 4 h. The first hour was for dark adsorption and the last 3 h was for light irradiation. The sample was taken every 30 min interval and the catalyst was then separated out from the solution. The solution was analyzed by UV-vis spectrophotometry. According to the Beer Lambert's law relationship in Eq. 3.4, the concentration of solution (c) is proportional to the light absorption of solution (A).

$$A = \varepsilon c l \tag{3.4}$$

where l is the path length of the sample (cm) and ε is molar absorptivity ($l.mol^{-1}cm^{-1}$), so the term of εl is constant throughout the UV-vis range

The activities of Ag_3VO_4, $CoTiO_3$ and its composite are shown in a relative concentration (C/C_0), where C is a concentration at every 30 min interval and C_0 is the initial concentration of MB. The performances of each catalysts are shown in Fig. 3.6.

The photocatalytic activity for MB degradation is found in a following order: 50% AV/CT > AV > 90% AV/CT > 70% AV/CT > 30% AV/CT > 50% AV+CT (Physical mixture) > 10% AV/CT > CT > photolysis. The highest activity is observed from 50%

AV/CT composite, indicating that this composition is the optimum content for methylene blue degradation.

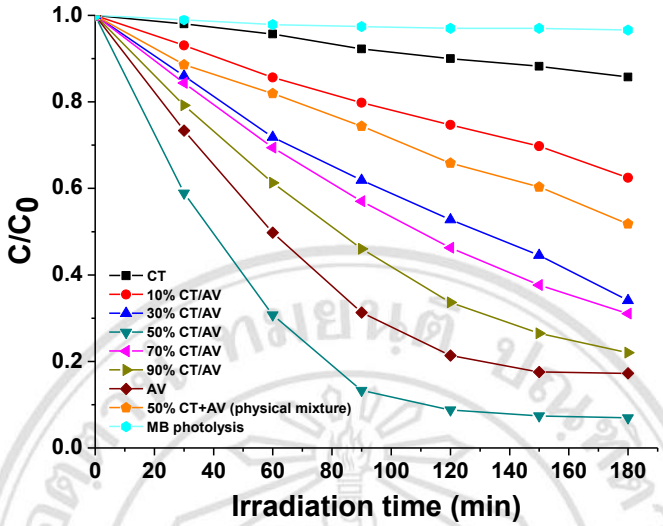

Fig. 3.6 Photocatalytic MB degradation activities under visible light irradiation.

The rate constant of degradation reaction can be determined by the relation in Eq. 3.5 according to the pseudo first order reaction. Therefore, the rate constant can be obtained from slope of the plot between $\ln(C/C_0)$ and irradiation time (min) in Fig. 3.7 [15].

$$\ln\left(\frac{C_t}{C_0}\right) = -kt \tag{3.5}$$

From the figure, the main component playing an important role in MB degradation is Ag_3VO_4 owing to its higher specific surface area (SSA) than that of $CoTiO_3$ from BET surface area determination (see section 3.1.5), so it is possible that more active sites are available for Ag_3VO_4 than $CoTiO_3$. Moreover, Ag_3VO_4 has less recombination process than $CoTiO_3$ which can be observed from low intensity of PL spectra compared with $CoTiO_3$ (see section 3.1.8). Therefore, increasing Ag_3VO_4 amount would probably lead to high activity. Although, $CoTiO_3$ is not quite active to MB degradation, coupling Ag_3VO_4 with an optimum amount of $CoTiO_3$ can provide the composite with a promising performance. Therefore, the role of $CoTiO_3$ in composite should be further investigated (see section 3.3).

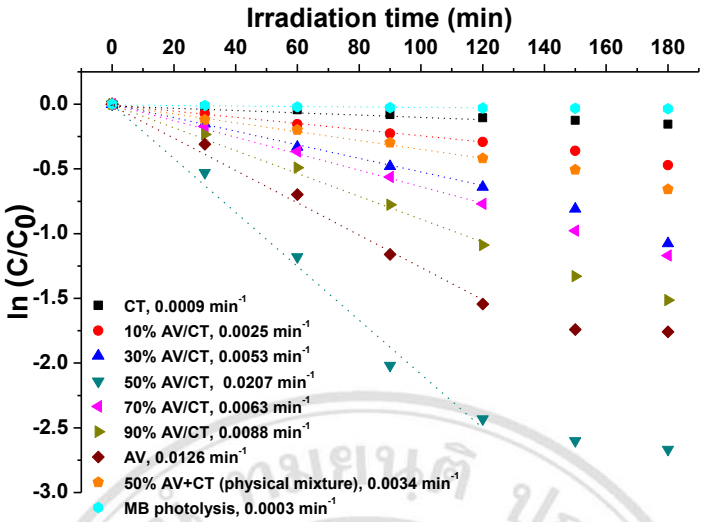

Fig. 3.7 The plot between $\ln(C/C_0)$ and irradiation time (min) according to pseudo-first order assumption.

In addition, 50% AV + CT physical mixture is also studied. This catalyst was prepared by mixing Ag_3VO_4 and $CoTiO_3$ in 1:1 weight ratio. The result shows that the activity of 50% CT/AV is apparently superior to that of 50% AV + CT physical mixture. This suggests that the strong interaction between Ag_3VO_4 and $CoTiO_3$ in the composite plays an important role in improving photoactivity. This strong interaction occurred via hydrothermal preparation is considered as chemical interaction involving in the electron-hole transferring process.

3.1.4 UV-vis diffuse reflectance spectroscopy (UV-vis DRS)

The band gap energy of photocatalysts can be measured by UV-vis DRS. The UV-vis DRS will detect the reflectance of a sample relative to that of the standard material ($BaSO_4$). This measured reflectance (R_∞) can be converted into absorption function $F(R_\infty)$ according to Kubelka-Munk equation (Eq. 3.6), which is normally used to describe behavior of light travelling inside a light scattering specimen.

$$F(R_\infty) = \frac{(1-R_\infty)^2}{2R_\infty} \tag{3.6}$$

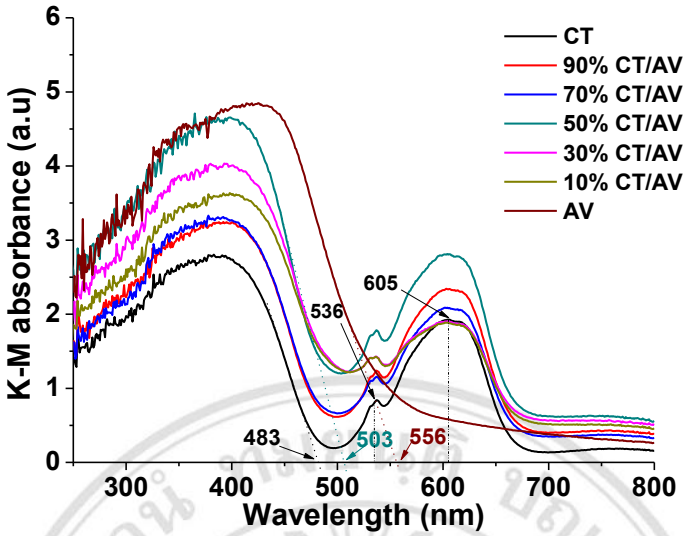

Fig. 3.8 The plot between Kubelka-Munk absorbance and light irradiation wavelength of Ag_3VO_4, $CoTiO_3$ and composites.

The plot between Kubelka-Munk absorbance and wavelength is illustrated in Fig. 3.8. The band gap calculation can be obtained by converting the absorption edge into energy using Eq. 3.7. The absorption edge and band gap energy of different coupling ratios are summarized in Table 3.3 [16].

$$E = \frac{h\upsilon}{\lambda} \quad \text{or} \quad E(eV) = \frac{1240}{\lambda(nm)} \tag{3.7}$$

Table 3.3 A summary of the absorption edge and the calculated band gap energy of different $Ag_3VO_4/CoTiO_3$ coupling systems.

Photocatalysts	Adsorption edge (nm)	Band gap energy (eV)
CT	483	2.56
10% AV/CT	494	2.51
30% AV/CT	495	2.51
50% AV/CT	503	2.47
70% AV/CT	511	2.43
90% AV/CT	518	2.39
AV	556	2.23

Table 3.3 shows the band gap energies of Ag_3VO_4, $CoTiO_3$ and composites. It is found that Ag_3VO_4 has the narrowest band gap, while $CoTiO_3$ has the largest band gap. The

results correspond to the photocatalytic activity study in which Ag_3VO_4 significantly shows higher activity than $CoTiO_3$. Therefore, when amount of Ag_3VO_4 is increased in composites, the reduction of band gap energy can be observed. Although, the 50% $Ag_3VO_4/CoTiO_3$ composite has wider band gap energy than pure Ag_3VO_4, it gives higher activity than Ag_3VO_4. This suggests that $CoTiO_3$ helps improve Ag_3VO_4 activity. It is possible that $CoTiO_3$ helps increase light absorption since it has two broad band absorption spectra in visible light region (500-700 nm) apart from the band absorption in UV region with an absorption edge at 483 nm. Thereby, $CoTiO_3$ could help increase the probability of visible light absorption.

The absorption edge of $CoTiO_3$ at about 483 nm accords with oxygen-metal charge transfer, OMCT ($O^{2-} \rightarrow Ti^{4+}$ transition) which relates to a direct band gap transition in the semiconductor. Whilst, the band in visible light region is ascribed to *d-d* transfer in Co^{2+} specie ($Co^{2+} \rightarrow Co^{2+}$ transition) which is ascribed to an indirect band gap transition [3-4, 17-18]. In visible light region, two absorption bands centered at 536 and 605 nm are due to the presence of tetrahedral Co^{2+} (d^7) species in $CoTiO_3$ structure. From the Orgel diagram in Fig. 3.9, the crystal field splitting of ground term and all terms of the same multiplicity is shown. The energy diagram of tetrahedral for d^7 configuration is shown on the left side of the diagram which arises from free-ion ^4F or ^4P terms. There are possible three transitions: $^4A_2(F) \rightarrow {}^4T_2(F)$, $^4A_2(F) \rightarrow {}^4T_1(F)$ and $^4A_2(F) \rightarrow {}^4T_1(P)$. The last two transitions require higher energy. Therefore, the intensity of the last two bands would be very low in UV-vis DRS spectrum [19]. Although, its *d-d* transition being one of forbidden transition rules, the effect of the spin-orbit coupling might help increase this *d-d* transition. Therefore, the band due to this transition can be more intense [20]. The spin-orbit coupling is a magnetic interaction aroused from a coupling between the orbital- and spin- angular momenta (*j*) of electrons which means that neither spin nor orbital properties are constant with time. The spin-orbit coupling occurs in 4d and 5d orbitals because of its unregulated electron distribution. As a result, the *d-d* transition can be obviously observed. Therefore, the UV region absorption band at 483 nm corresponds to $^4A_2(F) \rightarrow {}^4T_2(F)$ transition, while the two bands in visible region centered at 536 and 605 nm relate to $^4A_2(F) \rightarrow {}^4T_1(F)$ and $^4A_2(F) \rightarrow {}^4T_1(P)$ transitions, respectively.

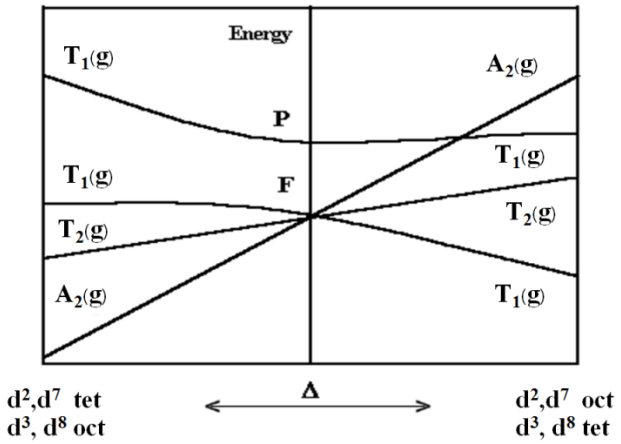

Fig. 3.9 Splitting of free-ion F and P terms in octahedral and tetrahedral fields [15].

3.1.5 Brunauer Emmett Teller method (BET)

The specific surface areas (SSAs) of semiconductor photocatalysts are determined by using a BET method. In this experiment, the SSAs of $CoTiO_3$, Ag_3VO_4 and the best composite catalyst (50% $Ag_3VO_4/CoTiO_3$) are compared as shown in Table 3.4.

Table 3.4 Comparison of the BET SSAs of each catalysts.

Catalysts	**Specific surface area (m^2/g)**
Ag_3VO_4	8.39
10% $Ag_3VO_4/CoTiO_3$	8.12
30% $Ag_3VO_4/CoTiO_3$	7.54
50% $Ag_3VO_4/CoTiO_3$	6.86
70% $Ag_3VO_4/CoTiO_3$	6.23
90% $Ag_3VO_4/CoTiO_3$	7.21
$CoTiO_3$	7.28

As seen from the table, Ag_3VO_4 shows the highest SSA which is consistent with the SEM measurement in which Ag_3VO_4 exhibits very small particle size in the range of micrometers. $CoTiO_3$ shows less SSA value than Ag_3VO_4 due to its bigger particle size, while the various ratios of $Ag_3VO_4/CoTiO_3$ show a decrease of SSAs when increasing the amount of Ag_3VO_4 in composite. It is possible that the increase content of Ag_3VO_4 leads to the agglomerated Ag_3VO_4 particles at the outer surface of $CoTiO_3$, thus reducing the active site at the surface. Nevertheless, the SSA is not significantly

different in each catalysts. SSA results are also not correlated with the activity testing, so it can be concluded that the surface area of photocatalysts in this system is not a main factor affecting the improvement of photocatalytic activity.

3.1.6 Fourier Transform Infrared Spectroscopy (FTIR)

FTIR is used to confirm the structure and bond formation in semiconductor photocatalysts. The wave number positions related to the bonding interactions are identified and presented in Table 3.5 and Fig. 3.10.

Table 3.5 Stretching and bending modes of Ag_3VO_4 [21-23] and $CoTiO_3$ with theirs corresponding wave numbers [3-5,13,16,14-26].

Wavenumber (cm^{-1})	**$CoTiO_3$**	**Wavenumber (cm^{-1})**	**Ag_3VO_4**
446	ν(Co–O–Ti)	502	Symmetrical ν(V–O–V) bridge of $V_2O_7^{4-}$
535	ν(Co–O)	608	Asymmetrical ν(V–O–V) bridge of $V_2O_7^{4-}$
619	ν(Ti–O)	672	Asymmetrical ν(V–O–V) bridge of VO_4
710	ν(Ti–O–R)	719	Symmetrical ν(V–O–V) bridge of VO_4
1605	ν(C–O) of acetate ion	852	ν(V–O–Ag)
		923	Symmetrical ν(V–O) terminal VO_3
		966	Asymmetrical ν(V–O) terminal VO_3
		1385	Organic residue impurity, δ(C–H)
		1454	Organic residue impurity, δ(C–H)
		1668	Organic residue impurity, ν(C=O)

For IR characterization, mid- and far-infrared region (1300 to 10 cm^{-1}) are interested in this study since these regions is the fingerprint as in the range of inorganic compound studied [27].

It can be seen from IR spectrum of $CoTiO_3$ in Fig. 3.10 that there are some impurities in the material which are consistent with the ν(Ti–O–R) at 710 cm^{-1} of residue organic solvent and ν(C–O) at 1605 cm^{-1} of acetate ion precursor. In Ag_3VO_4 spectrum, the trace of impurity is found from ν(V–O–V) bridge of $V_2O_7^{4-}$ at 502 and 608 cm^{-1} which is symmetrical and asymmetrical stretching, respectively. In addition, at 923 and 966 cm^{-1} corresponding with ν(V–O) terminal VO_3 is observed which can be occurred in condensation of VO_4^{3-} tetrahedral. Some organic residues in the range higher than 1300 cm^{-1} of Ag_3VO_4 may be due to the sample preparation procedure. The composite composes of both bonding interaction from $CoTiO_3$ and Ag_3VO_4 with a shift to lower wave number due to bonding formation between two semiconductors.

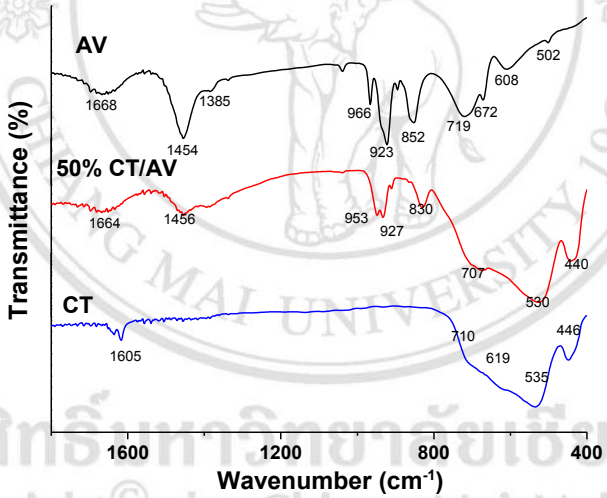

Fig. 3.10 Infrared transmittance band of each constituent and their composite.

3.1.7 Transmission electron microscopy (TEM)

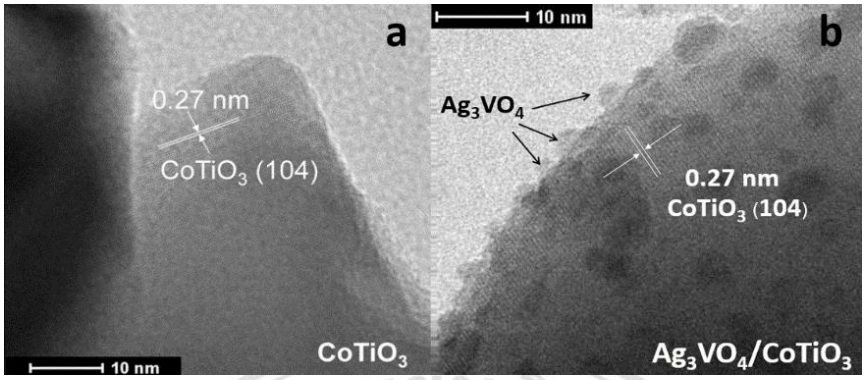

Fig. 3.11 TEM images of $CoTiO_3$ (a) and composite (b) with the lattice fringes related to (104) plane of $CoTiO_3$ [28].

TEM images apparently show an interaction between $CoTiO_3$ and Ag_3VO_4 heterojunction. From Fig. 3.11(a), the distance between lattice fringe is related to the strongest intense peak in the JCPDS pattern of $CoTiO_3$ which is (104) plane. The surface of $CoTiO_3$ is found to be rather smooth. The similar plane of $CoTiO_3$ is also observed in Fig. 3.11(b) of the composite material. The presence of rough surface is ascribed to a deposition of small Ag_3VO_4 particles on the $CoTiO_3$. The lattice fringe of Ag_3VO_4 cannot be detected from TEM analysis owing to a low stability of material under high electron beam energy. The change from smooth to rough surfaces is indicative of the close interfacial contact between Ag_3VO_4 and $CoTiO_3$ at the heterostructured interface.

3.1.8 Photoluminescence (PL)

The laser source with excited wavelength at 345 nm is used to activate the ground state electron in solid powder of semiconductor photocatalysts, resulting in an excited electron in the excited state. The signal is then detected from the emission fluorescence which occurs upon a deactivation of the excited electron back to ground state. Due to several vibrational energy levels in an excited state, the band in PL spectra can be broadened as illustrated in Fig. 3.12.

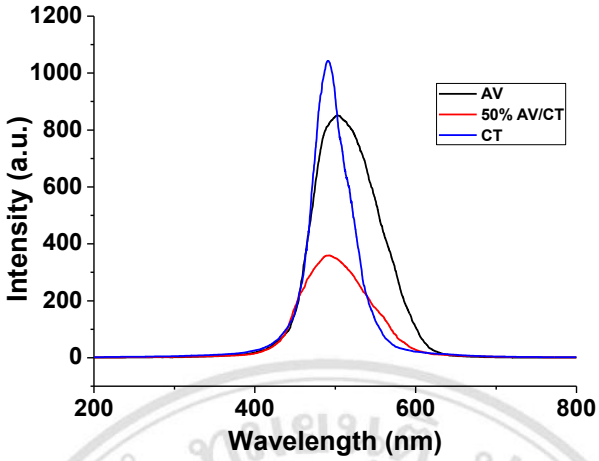

Fig. 3.12 Photoluminescence study of pure Ag_3VO_4, pure $CoTiO_3$ and composite system upon laser excitation at 345 nm.

In this research, the PL characterization is used for studying the recombination ability of semiconductors. The high intensity band refers to high recombination process because more excited electrons are deactivated. This recombination rate will suppress the photocatalytic activity of a semiconductor since the photoexcited electron would rather recombine with the photogenerated hole, than react with water molecules, oxygen molecules or hydroxide ion to produce the active species used in the organic pollutant degradation. The results show the lower PL intensity in the case of 50% $Ag_3VO_4/CoTiO_3$ compared with pure Ag_3VO_4 and $CoTiO_3$. This indicates that less excited electrons are deactivated, probably due to the presence of charge transfer between Ag_3VO_4 and $CoTiO_3$. The results clearly show that although $CoTiO_3$ and Ag_3VO_4 have high electron-hole recombination rate, coupling between the two materials can significantly reduce the process, hence high photocatalytic activity can be attained.

3.1.9 X-ray fluorescence analysis (XRF)

Since 50% $Ag_3VO_4/CoTiO_3$ composition shows the highest photocatalytic activity, the quantitative and qualitative compositions should be investigated. The signal of XRF is generated from the movement of outer level electron into the inner vacant shell leading to emission of characteristic radiation X-rays of definite wavelength. This emission wavelength is separated by reflection on the crystal when the Bragg's equation is fulfilled (see section 2.4.8). The composite is composed of aluminum, silicon, calcium,

titanium, vanadium, cobalt and silver in different weight percentages as presented in Table 3.6.

Table 3.6 Elemental analysis of composite material of 50% $Ag_3VO_4/CoTiO_3$ from XRF meansurement.

Component elements	**Amount of elements (wt %)**
Al	0.5250
Si	0.5561
Ca	0.2606
Ti	29.8056
V	4.7618
Co	38.1106
Ag	25.9804

In the preparation of composite material, 1 g of $CoTiO_3$ powder was added into the solution of $NaVO_3$ which is one of the precursor used for Ag_3VO_4. The $AgNO_3$ solution was then poured into the previous suspension to obtain 0.5 g as calculated. From the results in Table 3.6, the accurate compositional ratio between Ag_3VO_4 and $CoTiO_3$ in the 50% $Ag_3VO_4/CoTiO_3$ composite can be calculated from the ratio between Co and Ag elements.

According to the table, composite has Co element of 38.1106 g and Ag of 25.9804 g.

So, the Ag/Co weight ratio = $\frac{100 \times 25.9804}{38.1106} = 68.1711$ g

Therefore, the actual composition of the nominal 50% $Ag_3VO_4/CoTiO_3$ is 68% $Ag_3VO_4/CoTiO_3$. The difference from the nominal value is ascribed to the detection limit of XRF analysis. Since the XRF technique is a surface technique, an X-ray radiation could penetrate only within a few micrometer from the solid surface, so it is possible that the $CoTiO_3$ in the bulk is not exposed to the X-ray source, thus leading to low Co intensity.

3.2 The band alignment investigation by XPS technique and a proposed energy diagram with charge transfer of the coupling system.

XPS technique is used to examine the oxidation state of semiconductor photocatalyst. In addition, the binding energy shift can provide details on changes in chemical environments of atoms, therefore possible interaction between two semiconductors in composite can be confirmed. The XPS technique can also be used to determine energy level of valence band position in the vacuum scale, so the band alignment of the coupling system is proposed to explain the enhanced charge transfer process.

In pure Ag_3VO_4, the lowest binding energy found from Ag 3d orbital splits into two bands (Ag $3d_{5/2}$ and Ag $3d_{3/2}$) due to its spin-orbit coupling. The binding energy of Ag $3d_{5/2}$ at 368.0 ± 0.1 eV is composed of two main peaks at 367.9 ± 0.1 eV and 368.5 ± 0.1 eV which correspond to Ag^+ and Ag^0, respectively. The presence of Ag^0 in the spectrum is probably due to the reduction of Ag^+ since the species is light sensitive. For pure $CoTiO_3$ (Fig 3.13), the core level (CL) spectrum of Ti 2p state also splits into two peaks of Ti $2p_{3/2}$ and Ti $2p_{1/2}$. The binding energy of Ti $2p_{3/2}$ at 458.1 ± 0.1 eV consists of three components located at 458.1 ± 0.1 eV and 458.9 ± 0.1 eV for Ti^{4+} in $Co_xTi_{1-x}O_2$ and at 459.7 ± 0.1 eV for Ti^{4+}in bulk TiO_2 [29-32]. The Ag $3d_{5/2}$ of the composite material shows a positive shift of about 0.1 eV from the pure Ag_3VO_4 material. The two components of Ag $3d_{5/2}$ appear at 368.0 ± 0.1 and 368.6 ± 0.1 eV. Similarly, three Ti $2p_{3/2}$ sub-peaks of the composite are also shifted from those of pure $CoTiO_3$ about 0.1 eV to 458.2 ± 0.1 eV, 459.0 ± 0.1 eV and 459.8 ± 0.1 eV, respectively.

By plotting the intensity versus binding energy of valence spectra as shown in Fig. 3.13(e), the energy level position of valence band maximum (VBM) can be determined from the intersection between a linear fitted to the leading edge of the valence band spectrum and a linear fitted to the background. Kraut *et al*. [33] expressed the formulation to calculate the valence band offset (VBO, ΔE_V) which is based on the measurement of CL at the heterostructure interface and the separate measurement of the VB positions relative to the CL of each constituent material as shown in Eq. 3.8. In calculation of band alignment, CL of each material is chosen from the orbital with the lowest binding energy since this orbital is the closest orbital to the VB energy level of the material. The CL and VBM positions for the valence band offset calculation are

summarized in Table 3.7. The accuracy of the XPS peak position in the table is ±0.1 eV as evaluated by numerous fittings.

$$\Delta E_V = \left(E_{Ti2p}^{CoTiO_3} - E_{VBM}^{CoTiO_3}\right) - \left(E_{Ag3d}^{Ag_3VO_4} - E_{VBM}^{Ag_3VO_4}\right) + \Delta E_{CL} \qquad (3.8)$$

where $\left(E_{Ti2p}^{CoTiO_3} - E_{VBM}^{CoTiO_3}\right)$ is the energy difference between Ti 2p and VBM in pure $CoTiO_3$, $\left(E_{Ag3d}^{Ag_3VO_4} - E_{VBM}^{Ag_3VO_4}\right)$ is the energy difference between Ag 3d and VBM in pure Ag_3VO_4 and $\Delta E_{CL} = \left(E_{Ag3d}^{CoTiO_3/Ag_3VO_4} - E_{Ti2p}^{CoTiO_3/Ag_3VO_4}\right)$ is the energy difference between Ag 3d and Ti 2p CL peaks in $CoTiO_3/Ag_3VO_4$ heterojunction.

So, $\Delta E_V = \left(E_{Ti2p}^{CoTiO_3} - E_{VBM}^{CoTiO_3}\right) - \left(E_{Ag3d}^{Ag_3VO_4} - E_{VBM}^{Ag_3VO_4}\right) + \left(E_{Ag3d}^{CoTiO_3/Ag_3VO_4} - E_{Ti2p}^{CoTiO_3/Ag_3VO_4}\right)$

$$\Delta E_V = (458.1 - 1.4) - (368.0 - 1.6) + (368.1 - 458.2)$$

$$\Delta E_V = 0.2 \text{ eV}$$

Therefore, the VBO is approximately 0.2 eV, the conduction band offset (CBO) of heterostructure is then calculated by the following (Eq. 3.9) [33].

$$\Delta E_C = E_g^{Ag_3VO_4} - E_g^{CoTiO_3} - \Delta E_V \qquad (3.9)$$

From Eq. 3.9, both E_g values are the band gap energy of each component in composite material, which are obtained from UV-vis DRS characterization. The E_g of Ag_3VO_4 and $CoTiO_3$ are 2.2 eV and 2.6 eV, respectively. Therefore, substituting the obtained VBO in Eq. 3.9 will provide a CBO as shown below.

$$\Delta E_C = 2.2 - 2.6 - 0.2 = -0.6 \text{ eV}$$

The negative value of CBO means that the conduction band minimum (CBM) of Ag_3VO_4 is below that of $CoTiO_3$ [34-35]. From those values, the band alignment of $Ag_3VO_4/CoTiO_3$ system can be drawn as displayed in Fig. 3.14.

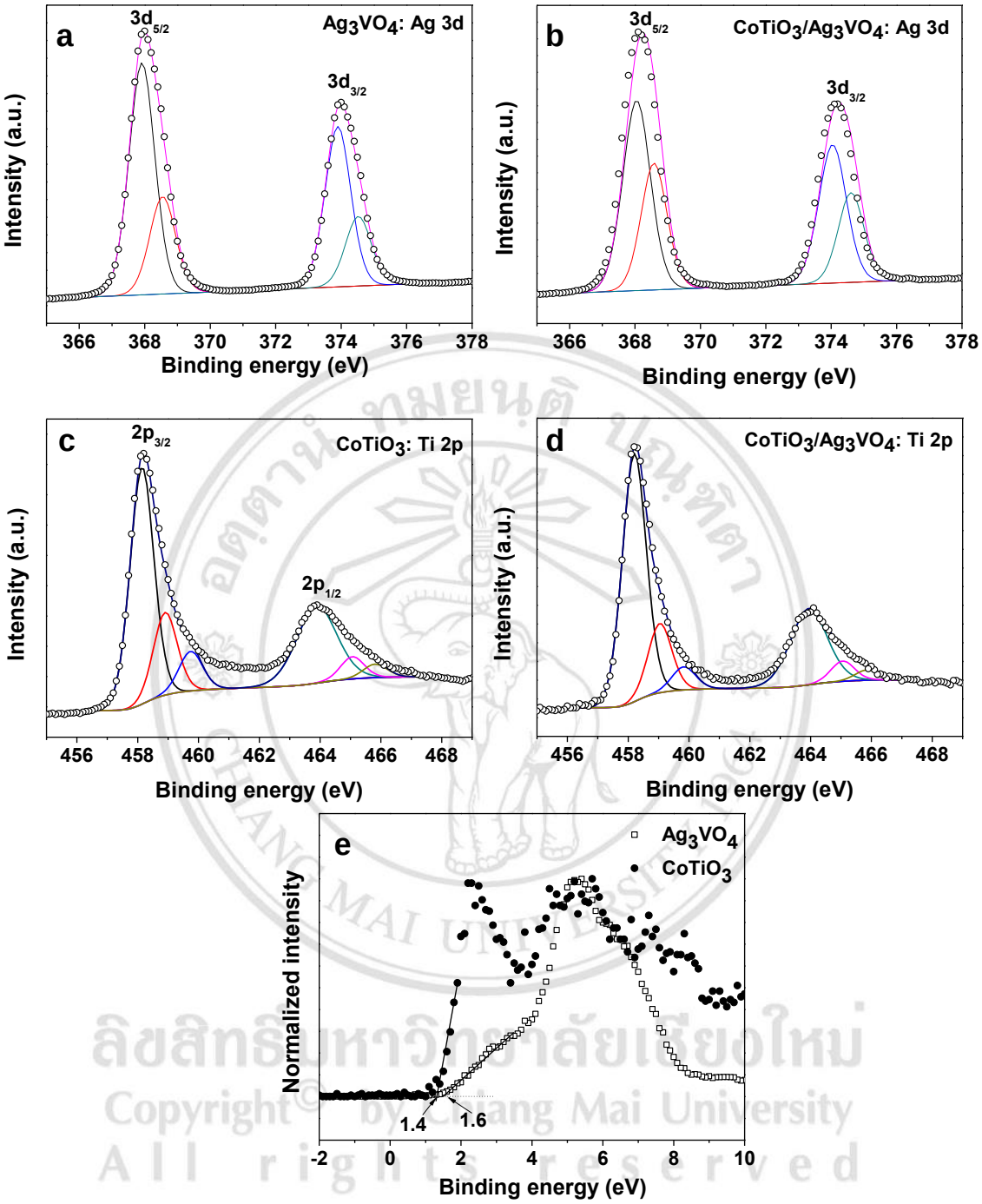

Fig. 3.13 XPS CL of Ag 3d in pure Ag_3VO_4 (a), Ag 3d in 50% $Ag_3VO_4/CoTiO_3$ (b), Ti 2p in pure $CoTiO_3$ (c), Ti 2p in 50% $Ag_3VO_4/CoTiO_3$ (d), and the VB spectra of each constituents.

Table 3.7 XPS CL peaks and VBM positions used to calculate the VBO of $Ag_3VO_4/CoTiO_3$ heterojunction.

Sample	Region	Binding energy (eV)
Ag_3VO_4	Ag $3d_{5/2}$	368.0 ± 0.1
	VBM	1.6 ± 0.1
$CoTiO_3$	Ti $2p_{3/2}$	458.1 ± 0.1
	VBM	1.4 ± 0.1
$CoTiO_3/Ag_3VO_4$	Ag $3d_{5/2}$	368.1 ± 0.1
	Ti $2p_{3/2}$	458.2 ± 0.1

The band structure of $Ag_3VO_4/CoTiO_3$ is considered to be type-II heterostructure. The charge transfer between the two materials can be drawn as in Fig. 3.14.

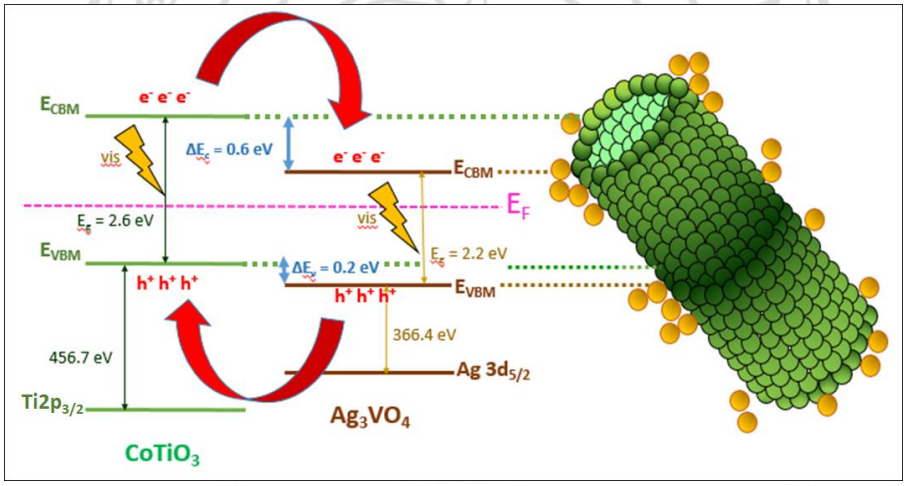

Fig. 3.14 Band alignment corresponding to type-II heterojunction and the proposed charge transfer diagram of $Ag_3VO_4/CoTiO_3$ system.

Fig. 3.14 shows the band alignment of $Ag_3VO_4/CoTiO_3$ system where a smaller band gap semiconductor (Ag_3VO_4) staggers the larger band gap semiconductor ($CoTiO_3$) which is considered as type-II heterostructure. The CBO equals to 0.6 eV, while VBO is 0.2 eV with VBM located at about 1.6 eV and 1.4 of Ag_3VO_4 and $CoTiO_3$ respectively. When the semiconductor is activated by visible light, the electrons from both Ag_3VO_4 and $CoTiO_3$ are excited from valence band (VB) to conduction band (CB), thus electron-hole pairs are generated. Due to higher positive potential energy of CB of Ag_3VO_4, the electrons on the CB of $CoTiO_3$ are transferred to the CB of Ag_3VO_4. In contrary, the holes on VB of Ag_3VO_4 can be transferred to VB of $CoTiO_3$ leading to

effective charge separation process. These separated electron-hole pairs can react with oxygen molecule, water molecules or hydroxide ion to further produce the active species enhancing the photocatalytic degradation. The efficient transfer of electron-hole pairs from the type-II band lineup also explains the enhanced photoactivity of the coupling system and corresponds to the reduction of peak intensity in PL spectrum of the composite material. Therefore, the improved catalytic performance of the composite is due to the reduction of charge recombination and an increase of the life time of photogenerated electron-hole pairs reacting to form active species.

3.3 The role of individual component and the main active species in $Ag_3VO_4/CoTiO_3$ heterostructure system

Due to the different mechanism of various photocatalyst systems, a clear understanding of the photocatalytic mechanism accompanied with the function of each constituent is important to further improve the novel photocatalyst. Therefore, an identification of the main active species of $Ag_3VO_4/CoTiO_3$ system and the investigation on the role of individual component that affects the improved photoactivity in the coupling system will be clarified in this section.

To understand the benefit of each component in the coupling system in improving photoactivity of the heterostructure, the light harvesting experiments are carried out. From the UV-vis DRS results in Fig. 3.8, it is found that broad absorption bands of $CoTiO_3$ component at 602 and 537 nm ascribed to $Co^{2+} \rightarrow Co^{2+}$ [4-5,14] is also found in the composite. These visible light region absorptions might help increase the light absorption range in the composite, leading to its improved photocatalytic activity. To verify the above assumption, two light filters (yellow and red) with different light cut-off ranges are used. The yellow filter is used to cut off the light wavelength below 510 nm, while the red one cuts off the light wavelength below 585 nm. The light cut-off range of each filter used is shown in Fig. 3.15. Different activities with and without filters are observed in Fig.3.16. The photocatalytic methylene blue degradation is decreased when using filter, since most of light activation range in the photoactivity process is cut off by the filter.

In the case of pure Ag_3VO_4, the main light activation range is already cut off by both yellow and red filters. Therefore, the degradation efficiencies in both conditions are nearly the same and no obvious effect of different light activation ranges is found.

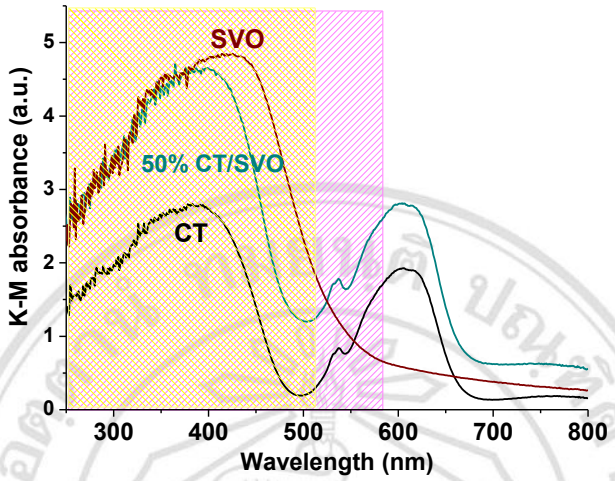

Fig. 3.15 The light cut-off ranges by yellow $(\lambda < 510$ cut off$)$ and red $(\lambda < 585$ cut off$)$ filter.

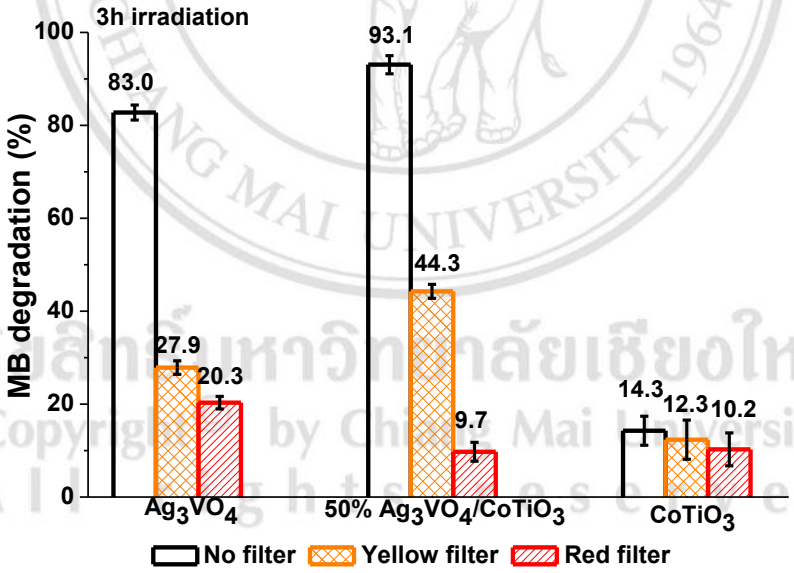

Fig. 3.16 MB degradation activity of photocatalysts with and without filter for 3 h irradiation.

However, the effects of red and yellow filters are more pronounced in the case of composite material. Although the yellow filter already cut out the main light activation range of Ag_3VO_4, the material is still able to absorb the light in the range higher than 500 nm owing to the visible light absorption of $CoTiO_3$ in composite material.

Therefore, the activity is higher than that of pure Ag_3VO_4 under the yellow filter used. However, when a red filter is applied, the activity is decreased since only the light in the range higher than 580 can be absorbed by the material. For $CoTiO_3$, the same activity as in the normal experiment is observed in all filters used due to its low photocatalytic activity. From the results, it can be concluded that $CoTiO_3$ component can help extend visible-light harvesting region of the heterostructure, although the individual activity of $CoTiO_3$ is very low.

From the photocatalytic studied, the charge transfer mechanisms for hybrid system with/without filter can be illustrated in Fig. 3.17. In normal condition, the transfer of electron-hole pairs is occurred in the similar manner as described previously. However, in the case of yellow filter experiment, less electrons are activated to generate electron-hole pairs, so only a few active species are produced which results in the decreased activity. Since there is less activation of Ag_3VO_4 component in the composite catalyst when yellow filter is applied, less holes in the VB of Ag_3VO_4 are transferred to the VB of $CoTiO_3$. Low catalytic activity is then observed. The production of electron at CB of $CoTiO_3$ is significantly reduced in the case of red filter, since only small part of $CoTiO_3$ component in the composite can be activated. Therefore, even lower activity is found in this case.

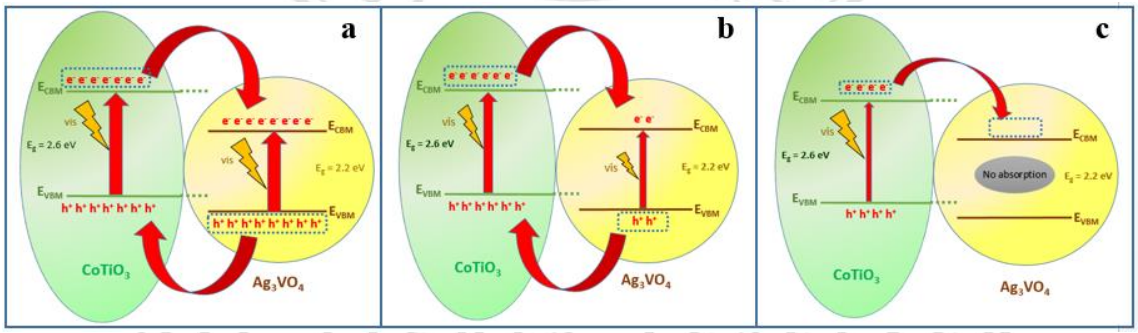

Fig. 3.17 Proposed charge transfer of coupling system between $Ag_3VO_4/CoTiO_3$ under normal light condition (a) and under cut-off filter; yellow filter (b), and red filter (c) respectively.

The role of each component as well as the active species in the catalytic system is further investigated by the in situ or indirect method where active species scavenger has been added into the photocatalytic reaction. The results are demonstrated in Fig. 3.18.

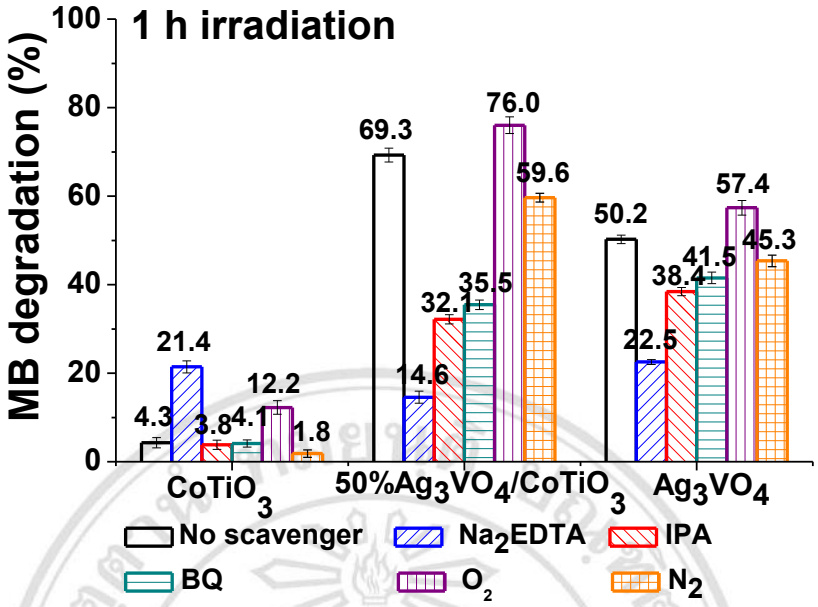

Fig. 3.18 Effect of active species scavenger on the photoactivity of the individual components and hybrid system.

Different scavengers used to trap different active species are shown in Table 3.8.

Table 3.8 Scavenger added for the specific active species trapping.

Scavenger type	**Trapped active species**
Ethylenediaminetetraaceticacid disodiumsalt (Na_2EDTA) [36-37]	h^+
2-propanol (IPA) [38-39]	$^{\bullet}OH$
p-benzoquinone [40-41]	$O_2^{\bullet-}$
O_2 [36,42]	e^-
N_2 [36,42]	Inhibitor of O_2

Instead of those scavengers in Table 3.8, other scavenger trappings which can be used are KI (h^+ and $^{\bullet}OH$ quencher) [43], and ethanol, isopropanol, methanol, ethylene glycol and acetone ($^{\bullet}OH$ quencher) [44-45].

Moreover, the $^{\bullet}OH$ can also be trapped by tert-butyl alcohol [42] with trapping of electron scavenger by using $AgNO_3$ [42] and $Cr_2O_7^{2-}$ [46], whereas hole is trapped by ammonium oxalate [42], acetate buffer [36] and triethanilamine [47].

As seen from Fig. 3.18, the MB degradation of $CoTiO_3$ is slightly decreased from 4.3% in normal condition to 3.8% and 4.1% when IPA and BQ were added respectively. Since high charge recombination rate of $CoTiO_3$ that obtained from high intensity of PL spectra leads to less charge transfer, so less active species were produced. Since there are only a few of $^{\cdot}OH$ and $O_2^{\bullet-}$ amount in the system, adding IPA and BQ scavengers has only less effect on MB degradation. On the contrary, a significant increase of MB degradation from 4.3% to 21.4% is found when adding Na_2EDTA, possibly due to hole trapping ability of Na_2EDTA in the system; hence less recombination process between electron-hole pairs are observed. The electrons in the system can react with oxygen molecules and consequently produce $O_2^{\bullet-}$ which is used in photocatalytic degradation, so the photoactivity is improved. This result is confirmed with O_2 and N_2 gases purging in the system. It is found that a rise of activity is apparent in the presence of O_2 while the reduced activity is found when O_2 is expelled by N_2 purging. This suggests that O_2 plays an important role in the MB degradation process and charge recombination in the $CoTiO_3$ system is dominant mechanism which overcomes the photocatalytic process.

For pure Ag_3VO_4 system, owing to its less recombination rate than that of $CoTiO_3$, the charge separation is better, resulting in various active species being produced in the system. When scavengers are added, photoactivities of Ag_3VO_4 system are obviously changed. The most clearly observed is found by adding hole scavenger. The activity is considerably dropped form 50.2% to 22.5% when Na_2EDTA presented in the system. A slight decrease is found in case of other scavengers (IPA and BQ). It can be implied that hydroxyl radical and superoxide radical are also participated in this system but showing less effect than holes. The effect of O_2 and N_2 purging is also not predominant. Therefore, the main active species for Ag_3VO_4 system is hole.

The composite material behaves similarly to Ag_3VO_4 system. By adding the scavengers in the system of 50% $Ag_3VO_4/CoTiO_3$, the activities are dramatically decreased from 69.3% to 14.6%, 32.1% and 35.5% for Na_2EDTA, IPA and BQ, respectively. The N_2 and O_2 purging experiment only points out the importance of the competing charge recombination process but with less extent than that in the pure $CoTiO_3$. Since the important scavenger that has the most effect on photoactivity is Na_2EDTA, the hole is found to be main species for MB degradation in 50% $Ag_3VO_4/CoTiO_3$ coupling system.

However, more pronounce effect is observed in the composite than that of Ag_3VO_4. It can be implied that this hybrid system has higher rate of active species formation. The high formation rate of active species is also apparently seen by the promising photoactivity of the 50% $Ag_3VO_4/CoTiO_3$ hybrid system which is further confirmed by PL characterization.

The catalyst (0.25) g was dispersed in the mixture solution of terephthalic acid 1.25 x 10^{-3} mol L^{-1} and sodium hydroxide 0.01 mol L^{-1}. The dispersed catalyst is stirred for 1 h for adsorption-desorption equilibrium. The same light excitation wavelength as in the photocatalytic study is then turned on for 1 h. The catalyst was separated from solution and the solution was analyzed by PL technique.

From the below mechanism, the hydroxyl radical produced under the photocatalytic condition can directly react with terephthalic acid to produce the fluorescence emission product of 2-hydroxy terephthalic acid which emits the florescence light at 426 nm [48]. This emitted fluorescence can be detected by PL technique. The intensity of fluorescence emission peak is proportional to the concentration of hydroxyl radicals produced in photocatalytic system [49].

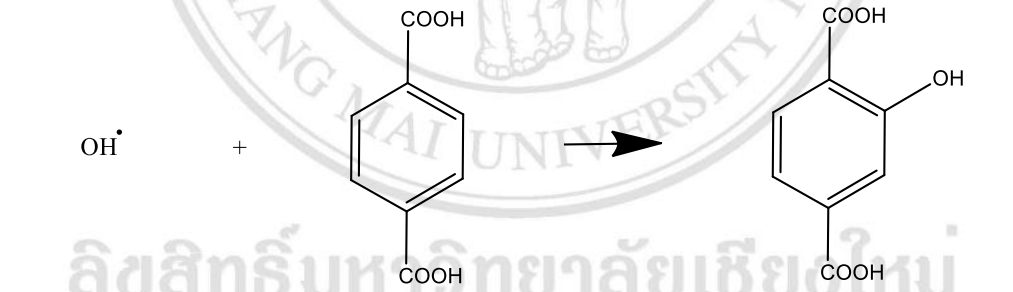

Hydroxyl radical | Terephthalic acid (TA) | 2-Hydroxy terephthalic acid (2-HTA) fluorescence emission at 426 nm

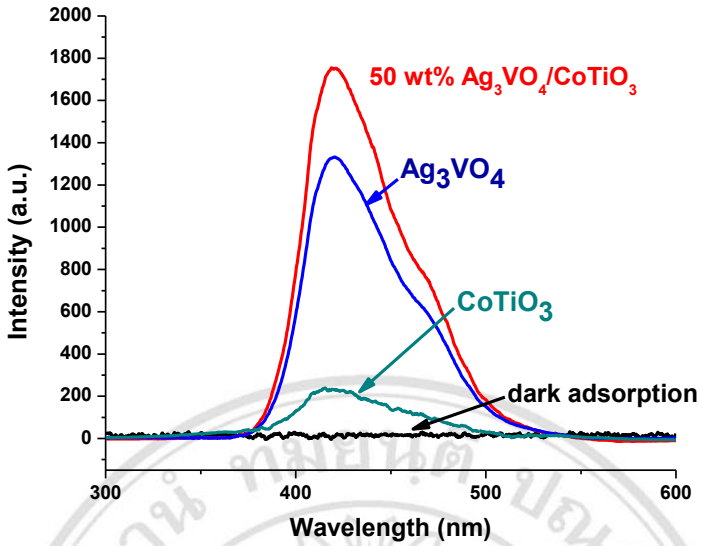

Fig. 3.19 Fluorescence emission spectra of 2-hydroxy terephthalic acid obtained from Ag_3VO_4, $CoTiO_3$ and the coupling system.

Fig. 3.19 shows the fluorescence emission spectra at 426 nm of 2-hydroxy terephthalic acid obtained from individual components and composite catalyst. The coupling system shows the highest fluorescence intensity, following by Ag_3VO_4 and $CoTiO_3$, respectively. The black line (catalyst testing under dark experiment) shows no emission peak, indicating no hydroxyl radical is produced. The strong and intense fluorescence emission peak found in the coupling system implies the fast rate of active species formation. This result suggests that the composite material can produce the higher amount of active species than Ag_3VO_4 and $CoTiO_3$, respectively.

REFERENCES

[1] S.-H. Chuang, R.-H. Gao, D.-Y. Wang, H.-P. Liu, Li.-M. Chen, and M. Y. Chiang, *Journal of the Chinese Chemical Society*, **57** (2010) 932.

[2] S.-H. Chuang, R.-H. Gao, K.-H. Gao, M. Y. Chiang, and T.-S. Chao, *Journal of the Chinese Chemical Society*, **57** (2010) 1022.

[3] Y.-J. Lin, Y.-H. Chang, W.-D. Yang, and B.-S. Tsai, *Journal of Non-Crystalline Solids*, **352** (2006) 789.

[4] M. K. Yadav, A. V. Kothari, and V. K. Gupta, *Dyes and Pigments*, **89** (2011) 149.

[5] Y. Qu, W. Zhou, and H. Fu, *ChemCatChem*, **6** (2014) 265.

[6] X. Hu, and C. Hu, *Journal of Solid State Chemistry*, **180** (2007) 725.

[7] G. Sun, H. Xu, H. Li, H. Shu, C. Liu, and Q. Zhang, *Reaction Kinetics Mechanisms and Catalysis*, **99** (2010) 471.

[8] A. T. Fisher, and M. B. Underwood, *Proceedings of the Ocean Drilling Program, Initial Reports*, **156** (1995) 29.

[9] N. P. Bansal, A. P. Singh, and H. Schneider,Innovative Processing and Synthesis of Ceramics, Glasses and Composites VIII, Ceramic Transaction 166, USA, 2004.

[10] A. Monshi, M. R. Foroughi, M. R. Monshi, *World Journal of Nano Science and Engineering*, **2** (2012) 154.

[11] W.-N. Wang, W. Widiyastuti, T. Ogi, I. W. Lenggoro, and K. Okuyama, Chemistry of Materials, **19** (2007) 1723.

[12] B. Akbari1, M. P. Tavandashti, and M. Zandrahimi, *Iranian Journal of Materials Science & Engineering*, **8** (2011) 48.

[13] D. Larcher, G. Sudant, R. Patrice, and J.-M. Tarascon, *Journal of Materials Chemistry*, **15** (2003) 3543.

[14] A. V. Vinogradov, V. V. Vinogradov, T. V. Gerasimova, and A. V. Agafonov, *Journal of Alloys and Compounds*, **543** (2012) 172.

[15] R. G. Mortimer, *Physical Chemistry 3rd edition*, Academic Press, London.

[16] N. Wetchakun, S. Chaiwichain, B. Inceesungvorn, K. Pingmuang, S. Phanichphant, A. I. Minett, and J. Chen, *ACS Applied Materials & Interfaces*, **4** (2012) 3718.

[17] G.-W. Zhou, D. K. Lee, Y. H. Kim, C.W. Kim, and Y. S. Kang, *Bulletin of the Korean Chemical Society*, **27** (2006) 368.

[18] A. Agui, and M. Mizumaki, *Journal of Electron Spectroscopy and Related Phenomena*, **184** (2011) 463.

[19] M.-W. Li, X.-M. Gao, Y.-L Hou, and C.-Y. Wang, *Journal of Nano- and Electronic Physics*, **5** (2013) 03022-1.

[20] M. Gerloch, and E. C. Constable, *Transition Metal Chemistry: The valence shell in d-block chemistry*, VCH press, Weinheim, New York.

[21] C.-M. Huang, G.-T. Pan, Y.-C. M. Li, M.-H. Li, T, and C.-K. Yang, *Applied Catalysis A: General* **358** (2009) 164.

[22] C. Belver, C. Adan, S. G.-Rodriguez, and M. F.-Garcia, *Chemical Engineering Journal* **224** (2013) 24.

[23] H. Tian, and I. E. Wachs, *Journal of Physical Chemistry B*, **109** (2005) 23491.

[24] M. Enhessari, S. N. Moqhadam, M. K. Razi, S. Ghezelbashi, and M. H. Tootkani, *International Journal of Nano Dimension*, **1** (2010) 125.

[25] P. D. Tsokov, V. N. Blaskov, Y. S. Stefanov, and T. M. Dobrev, *Journal of International Research Publication*, **1** (2006) 24.

[26] J. Luo, X. Xing, R. Yu, Q. Xing, D. Zhang, and X. Chen, *Journal of Alloys and Compounds* **402** (2005) 263.

[27] H. H. Willard, L. L. Merritt, and J. A. Dean, Instrumental Methods of Analysis: Fifth Edition, D. Van Nostrand Company, London, 1974.

[28] K. Wangkawong, D. Tantraviwat, S. Phanichphant, and B. Inceesungvorn, *Applied Surface Science* **324** (2015) 705.

[29] S. H. Lim, C. Ferraris, M. Schreyer, K. Shih, J.O. Leckie, and T.J. White, *Journal of Solid State Chemistry*, **180** (2007) 2905.

[30] S. Sharma, N. Thakur, R.K. Kotnala, and K.C. Verma, *Journal of Crystal Growth*, **321** (2011) 19.

[31] X. Xia, Z. Zeng, X. Li, Y. Zhang, J. Tu, N.C. Fan, H. Zhang, and H.J. Fan, *Nanoscale*, **5** (2013) 6040.

[32] J. F. Moulder, W.F. Stickle, P.E. Sobol, and K.D. Bomben, *Handbook of X-ray Photoelectron Spectroscopy: A Reference Book of Standard Spectra for Identificationand Interpretation of XPS Data*, Perkin-Elmer Corporation, Minnesota.

[33] E. A. Kraut, R.W. Grant, J.R. Waldrop, and S.P. Kowalczyk, *Physical Review A: Atomic, Molecular and Optical Physics*, **44** (1980) 1620.

[34] J. P. Bosco, S. B. Demers, G. M. Kimball, N. S. Lewis, and H. A. Atwater, *Journal of Applied Physics*, **112** (2012) 093703.

[35] S. Balaz, Z. Zeng, and L. J. Brillson, *Journal of Applied Physics*, **114** (2013) 183701.

[36] A. Cavicchioli, and I. G. R. Gutz, *Journal of the Brazilian Chemical Society*, **13** (2002) 441.

[37] X. Xu, X. Gao, Z. Cui, X. Liu, and X. Zhang, *Dalton Transactions*, **35** (2014) 13424.

[38] Q. G. Mulazzani, M. D. Angelantonlo, N. Camaloni, and M. Venturi, *Journal of the Chemical Society, Faraday Transactions*, **87** (1991) 2179.

[39] E. J. Feltham, M. J. Almond, G. Marston, K. S. Wiltshire, and N. Goldberg, *Spectrochimica Acta Part A*, **56** (2000) 2589.

[40] S. Lin, Z. Xin, M. Y.-Kun, L. M.-Yu, and Z. X.-Long, *Journal of Central South University*, **20** (2013) 495.

[41] A. Fattahi, S. R. Kass, J. F. Liebman, M. Agostinha, R. Matos, M. S. Miranda, and V. M. F. Morais, *Journal of the American Chemical Society*, **127** (2005) 6116.

[42] W. Li, D. Li, J. Wang, Y. Shao, J. You, and F. Teng, *Journal of Molecular Catalysis A: Chemical*, **380** (2013) 10.

[43] S. Wang, D. Li, C. Sun, S. Yang, Y. Guan, and H. He, *Applied Catalysis B: Environmental*, **144** (2014) 885.

[44] L. Zhang, Y. He, P. Ye, Y. Wu, and T. Wu, *Journal of Alloys and Compounds*, **549** (2013) 105.

[45] X. Hu, and C. Hu, *Journal of Chemical Technology and Biotechnology*, **85** (2010) 1522.

[46] S. Lin, Z. Xin, M. Y.-Kun, L. M.-Yu, and Z. X.-Long, *Journal of Central South University of Technology*, **20** (2013) 495.

[47] B. Ohtani, *Catalysts*, **3** (2013) 942.

[48] S. B. Rawal, D. P. Ojha, Y. S. Choi, and W. I. Lee, *Bulletin of the Korean Chemical Society*, **35** (2014) 913.

[49] T. B. Li, G. Chen, C. Zhou, Z. Y. Shen, R. C. Jin, and J. X. Sun, *Dalton Transactions*, **40** (2011) 6751.